Chapter

Terahertz Nano-Imaging with s-SNOM

Matthias M. Wiecha, Amin Soltani and Hartmut G. Roskos

Abstract

Spectroscopy and imaging with terahertz radiation propagating in free space suffer from the poor spatial resolution which is a consequence of the comparatively large wavelength of the radiation (300 μm at 1 THz in vacuum) in combination with the Abbe diffraction limit of focusing. A way to overcome this limitation is the application of near-field techniques. In this chapter, we focus on one of them, scattering-type Scanning Near-field Optical Microscopy (s-SNOM) which – due to its versatility – has come to prominence in recent years. This technique enables a spatial resolution on the sub-100-nm length scale independent of the wavelength. We provide an overview of the state-of-the-art of this imaging and spectroscopy modality, and describe a few selected application examples in more detail.

Keywords: Terahertz, near-field microscopy, s-SNOM, sub-wavelength spatial resolution, THz imaging, Drude conductivity model, plasma waves

1. Introduction

This article deals with THz s-SNOM. The abbreviation stands for Terahertz Scattering-type Scanning-Type Near-Field Optical Microscopy. It is a fairly novel branch of s-SNOM nanoscale spectroscopy which uses terahertz (THz) radiation for the probing (and also excitation) of the interaction with the material under investigation. The THz regime of the electromagnetic spectrum ranges from 0.3 THz to 10 THz, and is situated between the microwave and infrared portions of the spectrum. Interestingly, the THz frequency regime played a significant role during the early development of the s-SNOM technique. Some of the first attempts at reaching spatial resolution much below the diffraction limit were made with THz radiation, at that time using a down-scaled and tapered coaxial line [1]. Inspiration had come at that time from Scanning Near-Field Optical Microscopy (SNOM) which had been invented in 1981 and uses a tapered waveguide, usually a metal-coated optical fiber, with a sub-wavelength diameter at its end, which is brought to within a sub-wavelength distance of the sample. The waveguide is either used for the local excitation of the sample and/or for the collection of radiation from the sample [2, 3]. For the generation of images, the sample is raster-scanned as in all variants of Scanning Probe Microscopy (SPM). This technique works fine with visible and near-infrared radiation, however at longer wavelengths, the throughput of the waveguide decreases drastically if one tries to maintain a spatial resolution as small as in the visible range. In the last decade of the last century, it was then recognized [4], that it is more efficient for near-field sensing with long-wavelength radiation to

utilize scattering from the sharp tip of a needle which is illuminated from the outside. As such a needle, it is convenient to employ the probe tip of an Atomic Force Microscope (AFM), as one can then obtain topographical information simultaneously with spectroscopic information. Combined with techniques – described below – to suppress detection of radiation which does not come from the tip (apex) of the needle, this led to the breakthrough of s-SNOM as a powerful near-field spectroscopic technique at the turn of the millennium.

THz radiation always played a role during the rise to prominence of the technique, although a minor one. For example, in 2008, one of the early landmark demonstrations of the usefulness of the s-SNOM technique was the characterization of the spatial profile of the doping density in a Si MOSFET at 2.54 THz (in addition to measurements in the IR) [5]. However, there was always the challenge of the weak scattering efficiency of the probe tip. It arises from the unfavorable ratio of 10^{-4} to 10^{-5} between the probe tip's diameter (typically less than 50 nm) and the diameter of the focal spot of the THz beam (hundreds of micrometers to several millimeters). This challenge contributed to a slow progress which one can discern for THz s-SNOM throughout much of the last two decades, if compared with the huge attention devoted to s-SNOM in the infrared spectral regime. However, the number of publications dealing with THz s-SNOM is rising recently because the THz frequency regime offers a wealth of physical phenomena to be studied.

We mention in passing that also considerable interest exists in the development of s-SNOM-related techniques for the microwave regime. This effort is mainly driven by the need for diagnostic instrumentation for microwave electronic circuits. Again, the first efforts date back to the beginning of the s-SNOM technique itself [6]. Today, this specialized field is known under the name Scanning Near-Field Microwave Microscopy (SMM). A characteristic approach to overcome the challenge of the large wavelength and the concomitant large diffraction-limited focal spot size is the use of the cantilever of the probe tip as a waveguide for the injection and the return of the microwave signal [7]. This is implemented also in commercial products, e.g. from Keysight Technologies. In the following, we will not address the special developments in this field, but only point out the extraordinary attention which is given to careful calibration of the measurement systems which is needed to obtain reliable information about the device-under-test [8].

We also mention briefly other variants of sub-wavelength THz microscopes (both apertureless and with nanoapertures) which are very successfully used in specialized research applications. A preeminent example of an apertureless field measurement technique is the THz sensing of objects-under-investigation which are placed onto an electro-optic (EO) crystal [9]. Here, the THz electric field under the objects is detected by electro-optic conversion in that crystal. The spatial resolution is ultimately determined by the diameter of the focused optical read-out beam, which is in the range of one to several micrometers. An aperture-based near-field technique is the performance of transmission measurements through single slits in thin metallic films [10]. The spatial resolution in one dimension is determined by the width of the slit. With special processes, nanometer-scale widths have been achieved [11]. In order to obtain a sufficiently strong transmittance through the narrow slit to allow for measurements with a good dynamic range, the length of the slit is usually chosen such that a standing-wave resonance occurs at the THz frequency band of interest [12]. With the strong confinement and plasmonic enhancement of the electric field of the radiation in the slit, it has become possible to detect the THz absorption by just a few molecules brought into the slit [13].

Finally, before putting our focus on the s-SNOM technique, we mention two THz near-field techniques which measure electrical currents. Both usually employ THz pulses and time-domain spectroscopy. One technique uses probe tips with

integrated photoconductive switches for the detection of electric fields [14]. The other, very novel technique represents an advanced version of Scanning Tunneling Microscopy (STM) and employs THz pulses to induce excitations in the sample which lead to a modification of the tunneling current [15, 16]. This is a very promising technique as it gives for the first time for THz spectroscopy access to the atomic length scale.

2. General aspects of s-SNOM

As stated above, the basis of every s-SNOM device is an Atomic Force Microscope (AFM), where a sharp tip scans the sample to obtain topographical images. s-SNOM now simply adds illumination of the tip-sample region, the radiation inducing a near-field interaction which is detected via the scattered radiation, as shown in **Figure 1**. The red spot indicates the tip-sample region which is illuminated with focused radiation whose electric field ($E_{incident}$) induces a near-field interaction of the tip apex (typical size <50 nm) and the sample. The scattered electric field $E_{scattered}$ contains information about the local dielectric function ε_{sample}. As shown here, one often detects – for practical reasons – the radiation back-scattered onto the beam path of the incoming radiation. The probe tip is in this case part of a cantilever, but recently, researchers also have begun to employ tips attached to a quartz tuning fork, as they are employed in near-field measurement systems which can operate both as AFM and STM systems [17–19]. There are two advantages in the usage of an AFM. One obtains a topographical image simultaneously with the optical near-field information of the sample, and the up-and-down dithering of the probe tip at a frequency Ω provides the basis for the suppression of signals from radiation which does not originate from the apex region of the tip.

Sophisticated interaction models [20–22] and electromagnetic simulations [23, 24] have been published which describe the details of the s-SNOM near-field interaction. The most basic of them, the well-known electrostatic point-dipole model [4, 25] continues to yield valuable qualitative (even semi-quantitative) insight into how the s-SNOM probes the local dielectric function of the sample beneath the tip. This model explains that s-SNOM probes not primarily the surface of the sample but mainly a small volume underneath it. The achieved spatial resolution basically scales with the tip apex geometry, leading to a spatial resolution of typically <50 nm. The resolution is largely independent of the radiation wavelength from optical frequencies [4, 26] down to the sub-THz range [27].

Mathematically, electromagnetic waves under near-field conditions are described as evanescent waves possessing complex wave vectors (k-vectors).

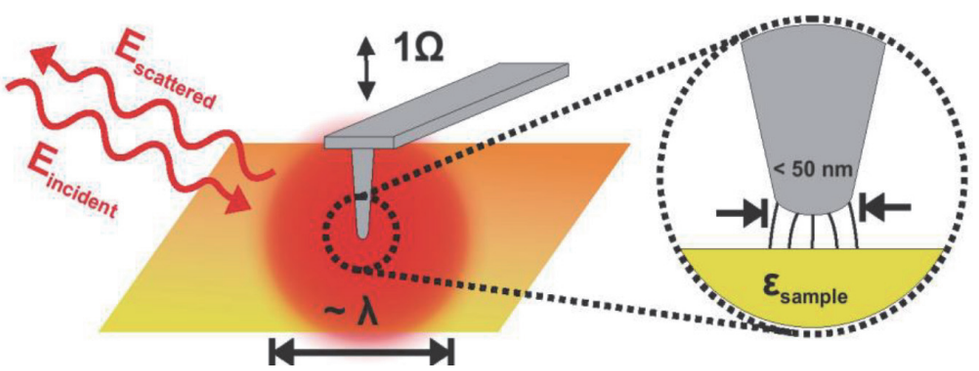

Figure 1.
Scheme of the s-SNOM technique. The AFM cantilever oscillates at a frequency Ω while the surface of the sample is scanned.

Formally, one can understand that sub-wavelength spatial resolution is possible in this case by considering momentum conservation as expressed in Eq. (1), where k_0 is the wave vector of the incoming wave. If one has an imaginary k-component in, e.g., z-direction (k_z), then this allows for large wave vector components in the xy-plane $k_{xy} > k_0$, hence a high spatial resolution in this plane [2, 28]:

$$k_0^2 = k_{xy}^2 + k_z^2 = k_{xy}^2 + (i|k_z|)^2 = k_{xy}^2 - |k_z|^2. \quad (1)$$

The big technical challenge of s-SNOM is already apparent in **Figure 1**. Not only the nanometer-sized tip apex is illuminated by radiation, but rather a spot with an area larger than the diffraction-limited spot size. This spot size scales with λ [2]. Therefore, the back-scattered light contains background light from the sample, tip, and cantilever. This unwanted radiation is much stronger than the desired near-field contribution. As the former cannot be eliminated by wavelength or polarization filtering, it must be suppressed during processing of the detected signal, which is done as follows:

The AFM is operated in the so-called non-contact mode, i.e. the tip oscillates at a frequency Ω close to its mechanical resonance frequency [29]. The different components of the scattered and reflected waves from the tip-sample region are affected in different ways by this oscillation, which allows to cancel their contributions by specific modulation-related filtering measures. A big background contribution arises from (far-field) reflection and scattering from the sample away from the tip apex, resulting in a constant DC term. In contrast, the signal from waves interacting with the oscillating tip away from its apex is modulated at the fundamental oscillation frequency 1 Ω. Finally, the near-field interaction between the tip apex and the sample imprints a higher-harmonic response onto the waves scattered from the apex region. This can be understood in the following way. An essential property of this interaction is its strong nonlinear dependence on the tip-sample distance z (e.g., for the aforementioned point-dipole model, the near-field signal scales with $E_{nf} \propto 1/(1 - bz^{-3})$). Therefore, decomposing the near-field signal from a harmonically oscillating tip (z = z0*sin(Ωt)) into its Fourier components leads to a Fourier series of higher harmonics. Hence, demodulation (i.e., extraction) of the measured back-scattered signal at higher harmonics (2 Ω, 3 Ω, … .) isolates the near-field part and suppresses the background [30, 31]. With an increasing order of the higher harmonic, the background suppression becomes better, but the signal strength decreases.

The detectors used for s-SNOM are power detectors. The detected electric field contains the near-field contribution E_{nf} with the phase ϕ_{nf}, and the background contribution E_b with the phase ϕ_b, which yields the total detected intensity

$$I \propto |E_b + E_{nf}|^2 = E_b^2 + E_{nf}^2 + 2|E_b||E_{nf}| \cos\left(\phi_{nf} - \phi_b\right). \quad (2)$$

The higher-harmonic demodulation suppresses the pure background term E_b^2 and, using the approximation $E_b \gg E_{nf}$, the pure near-field term E_{nf}^2 can be neglected as well. Hence, the term $s = 2|E_b||E_{nf}| cos\left(\phi_{nf} - \phi_b\right)$ is the outcome of the higher-harmonic demodulation. As desired, s is proportional to $|E_{nf}|$, but it also depends on the (uncontrollable) background $|E_b|$ and the relative phase between those fields. Hence, a change in the measured signal cannot be attributed unambiguously to the near-field wave, the background or the phase difference between them.

In order to overcome this problem, interferometric frequency-mixing techniques in addition to the higher-order demodulation have been introduced. They play an important role in s-SNOM data recording and processing. Essentially, a

3.1 Time-domain THz s-SNOM

THz Time-Domain Spectroscopy (THz-TDS) is one of the most widespread spectroscopic tools in THz science since it possesses many advantages [47]. It is based on the use of single- or few-cycle THz pulses whose waveforms are measured as a function of time by coherent detection with electro-optic (EO) crystals or photo-conductive antennas (PCAs). With these techniques, one often achieves a high signal-to-noise ratio. Both the amplitude and phase of the electric field of the radiation are recorded. This occurs over the entire spectrum of the pulses which is then available for the extraction of spectral information. Furthermore, high peak intensities are reached, which makes time-resolved pump-probe measurements possible. Its drawback is the poor diffraction-limited spatial resolution which lies in the millimeter regime. The s-SNOM technique can solve this issue and open the path into the nanoworld with sub-100-nm resolution. However, s-SNOM has the following limitation. As the tip oscillates at frequencies of tens to hundreds of kHz, the pulse repetition rate of the THz source must be in the MHz range in order to avoid synchronization challenges with the lock-in detection. Hence, only high-repetition-rate THz sources are employed until now, not amplifier-based systems.

Aligning a time-domain THz s-SNOM system is not trivial since the average beam power is low, on the order of μW, and the THz pulse durations are quite short, typically on the 1-ps time scale. For standard THz-TDS systems, one finds that a high signal-to-noise ratio (SNR) can only be achieved if the measurement system, especially the detection segment, is aligned near its optimum. The alignment of a THz s-SNOM is even more critical because only a small amount of radiation scattered from the probe tip can be detected. As estimated from the data in [17, 48, 49], the signal at the first harmonic 1Ω is reduced to 0.1–1% as compared with the signal obtained in conventional THz-TDS. Concerning the use of THz pulses with ps duration, it is a challenge to find the temporal overlap between the (weak) tip-scattered signal and the laser pulse used for EO detection or for activation of the PCA detector. Upon THz beam steering, the path length changes. In practice, an iterative alignment procedure is employed.

s-SNOM systems operating in the IR, near-IR or VIS preferably exhibit the back-reflection geometry of **Figure 2a**. Here, the scattered and impinging light are on the same side of the probe tip. A beam-splitter (shown in blue in **Figure 2a**) divides the incident light for probing the sample and interferometric detection. The pathway of the incoming radiation – including the focusing leg to the tip –.Time-domain THz s-SNOM systems more commonly use the transmission geometry of **Figure 2b**. The beam alignment is much simplified in this optical arrangement as one can pre-align it with the help of the laser beams used for the generation and detection of the THz pulses. No THz beam-splitter is required. Either a single big paraboloid mirror as in **Figure 2b** or two separate smaller ones are employed for the incoming and the

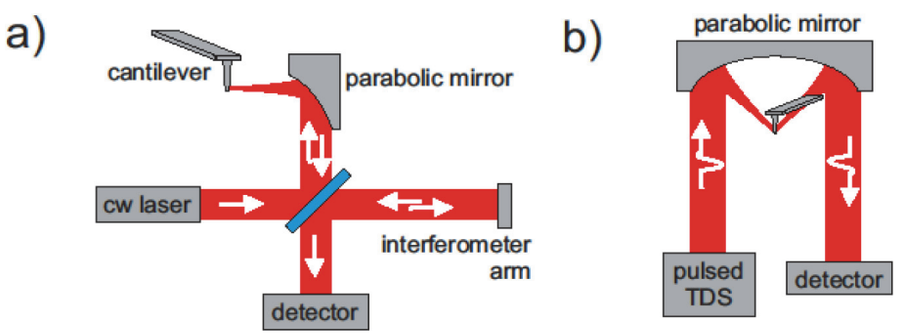

Figure 2.
s-SNOM modalities, (a) back-reflection and (b) transmission geometry.

back-scattered radiation. The coherent detection of the THz pulses, inherent of the THz-TDS approach of **Figure 2b**, eliminates the need for phase-sensitive interferometric detection as it shown in the setup of **Figure 2a**.

In TDS, the measurement of spectra usually requires translation of a mechanical delay stage, which varies the time delay between the scattered radiation pulse and the read-out laser pulse. For the IR region, the term of nano-FTIR (FTIR: Fourier Transform Infrared Spectroscopy) was introduced for this approach [38]. However, the recording of spatial maps across a sample region with full spectral information at each local position is so time-consuming that it is rarely done in the THz frequency range. Nowadays, it is still common to keep the time delay stage fixed at the position of maximal peak intensity during a spatial scan of the sample. This results in maps of the THz response which do not have frequency resolution [49, 50]. Full spectra are often recorded only at selected sample positions [50, 51]. Further improvements are expected because most concepts of time-resolved THz spectroscopy are compatible with s-SNOM, such as Asynchronous Optical Sampling (ASOPS), which does not require a mechanical translation stage for the measurement of spectra [48]. Again the infrared s-SNOM technology is more advanced, as highlighted by Ref. [52], where the propagation of phonon polaritons in hexagonal boron nitride was recorded in real space by time-resolved IR s-SNOM measurements.

3.2 CW THz s-SNOM

A second branch of THz s-SNOM uses continuous-wave (CW) technology. Without the need for finding temporal pulse overlap and with the high spectral power of the radiation, the measurement systems are easier to align than TDS-based systems. The rapid development of this sub-field of THz s-SNOM is reflected in an impressive technological diversity. As THz sources, large-scale facilities such as free-electron lasers (FELs) [53], but also THz gas lasers [5, 33], and compact tabletop electronic (frequency-multiplier-based) sources [27, 35, 54, 55] as well as quantum-cascade lasers (QCL) [19, 56, 57] are being used. The latter is operated in a CW mode, but novel phase-control techniques are currently developed to enable the use of the QCLs in pulsed mode [58]. On the detector side, the selection is limited since the detector must be sensitive and fast enough to resolve the higher harmonics $n\Omega$ of the cantilever frequency in the typical range of several tens to hundreds of kHz, which excludes Golay cells and slow bolometers. In the first years of THz s-SNOM, liquid-helium-cooled hot-electron bolometers were the standard solution [5, 53]. Recently, room-temperature-operated detectors such as Schottky diodes [33, 35, 55] and field-effect transistors [27] have emerged, facilitating the entire measurement procedure. Microbolometers also appear possible, but we are not aware of reports of their use. Finally, THz-QCLs are employed for both emission and detection because the laser light can be generated and measured in a single device [19, 56].

Interferometric detection schemes to achieve more reliable and phase-sensitive measurements become the preferred mode of operation of THz CW s-SNOM. The pseudo-heterodyne scheme as the state-of-the-art technology for s-SNOM in the IR and VIS spectral regimes is challenging to implement for THz radiation. Aiming for the same approach as in the IR/VIS, one would require a mirror oscillating at several hundred Hz with a displacement amplitude scaling with the wavelength [36], which is so demanding that it has not been realized so far. Other approaches appear possible for future use, such as a continuous mirror shift or the use of folded beams. Hence, nowadays, the following alternative interferometric detection schemes find application in CW THz s-SNOM:

- Non-interferometric "self-homodyne" detection is still in use [53], however the phase information is not accessible and this mode possesses the signal ambiguity discussed in conjunction with Eq. (2).

- As the simplest interferometric scheme, homodyne detection is widespread [27, 33]. It offers interferometric signal enhancement and phase sensitivity by two consecutive measurements (at the risk of errors by drifts and tip degeneration). Samples with limited or no optical phase variations across them can be mapped with a single spatial scan by adjusting the interferometer to the maximum signal position.

- Heterodyne detection [35, 55] requires two sources (the second one as local oscillator) and the requirements for the signal-demodulating lock-in amplifiers are high. This makes the approach comparatively cost-intensive, but one benefits from the maturity of heterodyning when working with frequency-stable electronic sources.

- New approaches such as synthetic optical holography (SOH) [59, 60], which relies on data post-processing, have been demonstrated successfully as well.

3.3 Probe tips for THz frequencies: length and shape

THz s-SNOM has also been improved on the basis of a deeper understanding of the fundamental role of the probing tip which acts as an antenna for the impinging radiation. For that reason, metallized tips are preferred; this is the case for IR and VIS radiation, but even more so at THz frequencies. Ref. [61] reports a nine times higher s-SNOM response if standard probe tips, which were developed for the IR, are replaced by longer THz-resonant ones. Nowadays one often finds commercially available Pt tips with a typical length of 80 μm [62] in use, even if they are not exactly resonant at the wavelength of the specific radiation. When self-etched metallic wires mounted on tuning forks [61] are employed, the length of the wires tends to be inadvertently well-suited for THz frequencies.

Another aspect is the tip apex geometry. Surprisingly, blunt tips show a better THz s-SNOM signal than sharp tips [33, 59]. This is explained by the increased interaction volume of the near-field zone to dominate over the reduction of the field enhancement. The loss in spatial resolution due to the bigger tip radius does not scale inversely with the signal gain. Ref. [33] reports a result with one order of magnitude higher THz near-field signal, but inducing a resolution degradation by only a factor of four. Still, one has to make a trade-off between resolution and signal strength.

Regarding the achievable spatial resolution, there seems to be a consensus that routine THz s-SNOM reaches a resolution of 50–100 nm. Best values of <15 nm were achieved in Ref. [33] with customized tips and a well-chosen oscillation amplitude and data averaging. One does not reach the atomic resolution while this is possible with THz-STM [15].

3.4 Ability of THz s-SNOM for depth probing

A new branch of s-SNOM research is dedicated to sub-surface imaging [17] and nano-tomography [63–65] by the analysis of the s-SNOM signals at different higher harmonics (2 Ω, 3 Ω, 4 Ω, … .). They probe the sample down to different depths [63–65]. By the combination of data taken at various harmonics, it is possible to determine depth profiles of specimens.

3.5 Timeline of technological advances of THz s-SNOM

For readers who are interested in a quick overview of important technical developments in THz s-SNOM, the following table presents a timeline of advances with respect to sources, detectors, achieved spatial resolution and other innovations listed under the category "Remarks". The first column specifies the respective reference and the year of its publication. The second column specifies the radiation source; the information "THz pulses" stands for the opto-electronic generation of THz pulses with femtosecond IR or VIS laser pulses. The list does not claim to be complete and only serves as a quick review of the overall development of THz s-SNOM.

4. Application examples of THz s-SNOM

In the following, we discuss four publications in more detail, which are representative for important applications of THz s-SNOM. The topics are the mapping of the conductivity of charge carriers (in Section 4.1), the mapping of surfaces of materials which undergo a phase transition (in Section 4.2), sub-surface imaging (in Section 4.3), and the probing of surface waves (in Section 4.4).

The objects-under-study of all examples are solid-state materials or device microstructures. Extension of THz s-SNOM to probe soft matter is expected in the near future. Similarly, the study of aqueous solutions [66] and biomedical, even alive [67] specimens will come. This will be accompanied with the appearance of modified measurement modalities. Similar developments have taken place in the IR spectral regime where AFM-IR was developed as a family of techniques. The probe tips of AFM-IR do not oscillate, instead acting as contact sensors for measuring thermal expansion induced by wavelength-selective excitation of the specimens [68].

4.1 Nano-imaging of semiconductors with spatially varying density of mobile charge carriers

Determination of the conductivity and of the charge carrier concentration, which is determined by the level of doping, is important for semiconductor technology. THz waves are much more sensitive than IR or VIS radiation for the non-destructive probing of dielectric contrast arising from the Drude conductivity of mobile charge carriers at a density in the range of $10^{16} - 10^{19}$ cm^{-3} (see below), which is the relevant range for semiconductor devices. Ref. [5] employed THz s-SNOM to image this contrast in electronic circuits with field-effect transistors. For that purpose, a processed semiconductor die was cut, and the side facet polished and subjected to s-SNOM imaging. The top panel of **Figure 3a** displays an AFM image. It provides little contrast and the transistor locations cannot be identified. This is possible, however, with the help of **Figure 3b**, which shows an SEM image of the sample. Based on the information from **Figure 3b**, the position of one of the transistors is marked in the top panel of **Figure 3a** by the black box. The two lower panels of **Figure 3a** display the data measured by s-SNOM, namely the 2nd-harmonic-demodulated near-field images recorded at 2.54 THz and 28 THz, respectively. The images exhibit very pronounced signal strength in the regions where one expects doping. The strength of the THz near-field signal is maximal at the device layer and continuously reduces away from the transistors towards the interior of the Si wafer. The decline in signal strength reproduces the gradual decrease of the carrier concentration whose local values (derived from device

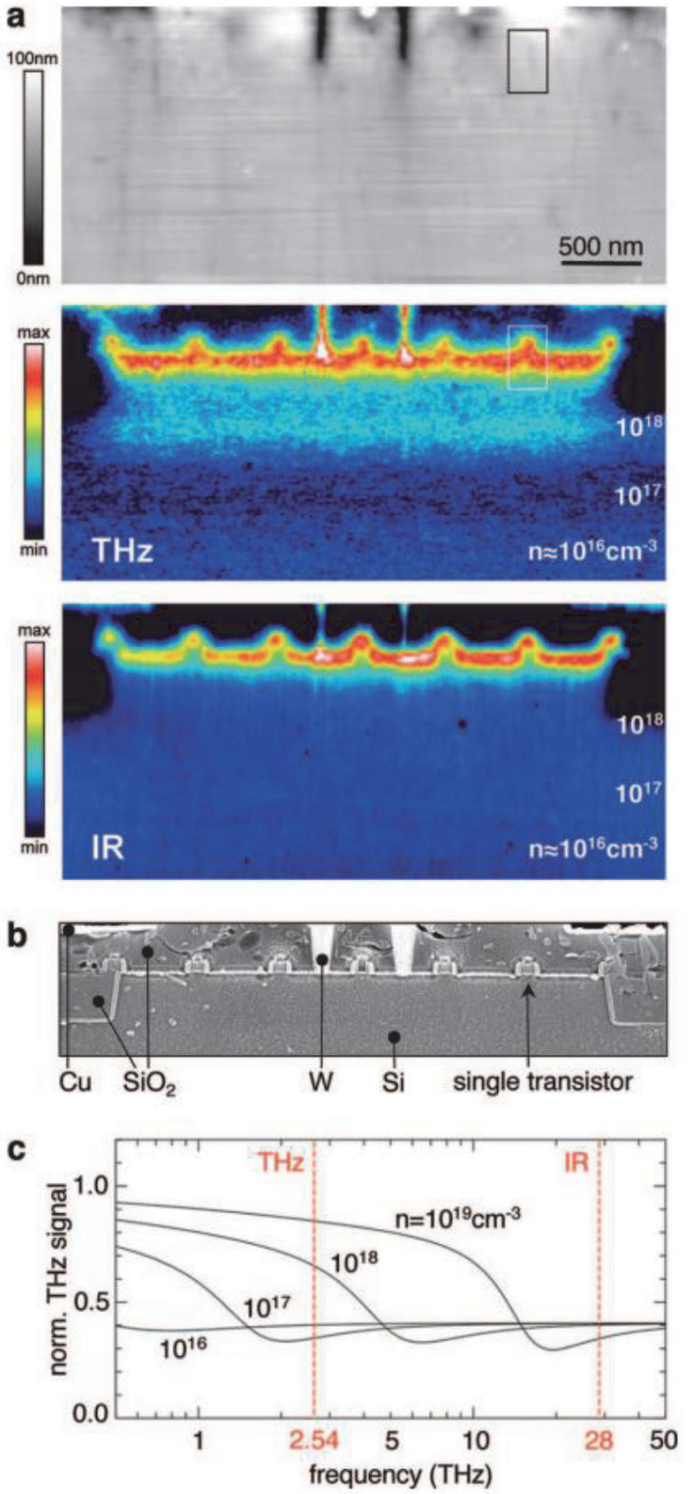

Figure 3.
(a) Three panels showing data measured by AFM (top), 2nd harmonic s-SNOM at 2.54 THz (middle) and 2nd harmonic s-SNOM at 28 THz, respectively. (b) SEM image of the sample surface. (c) Calculated s-SNOM near-field response as a function of charge carrier concentrations. Reprinted with permission from [5]. Copyright (2021) American Chemical Society.

simulations) are listed in the image plots. Compared to the 2.54-THz data, the IR data at 28 THz reproduce the continuous concentration decline only in the vicinity of the devices, but not further away from them. Obviously, IR s-SNOM is sensitive to high carrier concentrations, but not the low ones. **Figure 3c** displays modeled near-field data as a function of the carrier density. It shows the relative signal strength calculated with the point-dipole model for a Drude plasma in Si. The graph confirms that the near-field signal at 2.54 THz is sensitive to doping densities

throughout the range specified above. Ref. [5] points out that an average of less than 100 electrons in the probed volume suffices to evoke significant THz contrast. At 28 THz, only the highest densities in the 10^{19}-cm^{-3} range provide a signal sufficiently strong for concentration discrimination. Interestingly, the graph also explains why the 2.54-THz s-SNOM image exhibits a local minimum 900 nm below the transistor layer. The expected signal is minimal at a doping level of 10^{17} cm^{-3} and rises again with decreasing concentration. Finally, we note that THz s-SNOM has recently been used to identify both the carrier type (electrons or holes) and the carrier density [35].

4.2 Phase transitions

Another application of THz s-SNOM is the spatial mapping of phase transitions. Well-known literature examples deal with insulator–metal transitions (IMTs). THz s-SNOM measurements can detect the IMT and allow to decide whether it occurs simultaneously or percolatively across the sample. The measurements also permit to find out the temperature range of the IMT. THz s-SNOM furthermore makes it possible to investigate the formation and thermal evolution of metallic and insulating domains. As an example, Ref. [49] reported measurements of the response of vanadium dioxide at THz and Mid-IR frequencies as a function of temperature, while crossing the transition temperature, T_C, which lies somewhat above room temperature. **Figure 4** shows the demodulated 2nd-harmonic near-field signal measured with a THz TDS system without frequency resolution (top), and the demodulated 3rd-harmonic near-field response in the Mid-IR measured with a CO_2 laser source. The comparison of the results indicates that the signal change at THz frequencies extends over a larger temperature range than in the Mid-IR, where it is fairly abrupt. The Mid-IR data are consistent with a first-order phase transitions, while the THz data suggests a more complex mechanism than the previously assumed one. Besides, coexistence of both insulating and metallic domains are observed at THz and Mid-IR frequencies during the transition.

Another phase-sensing study was reported recently in Ref. [59]. It investigated the chalcogenide $Ge_1Sb_2Te_4$, a so-called phase-change material —a class of materials which is employed for nonvolatile rewritable data storage. Electric or optical pulses can switch these materials between an amorphous and a crystalline phase. In this study, an s-SNOM system with a molecular gas laser and a cryogenically cooled bolometer was used to distinguish the two phases at various frequencies from 1.89 THz to 5.67 THz. The s-SNOM contrast arises from the differences of the phonon spectra of the two phases. The study showed that phase discrimination is principally possible, which opens the way for more detailed studies of domains and of the kinetics of the phase transition.

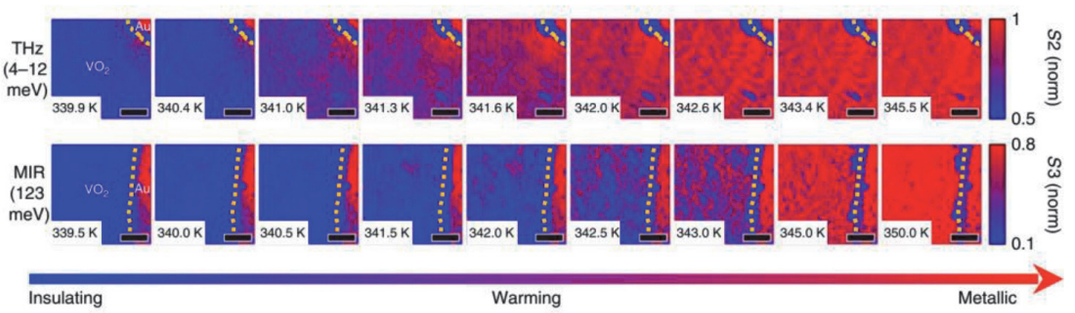

Figure 4.
Near-field mapping of a VO_2 surface during IMT. Measurements were performed as a function of temperature at THz frequencies (top panels) and in the mid-IR (bottom panels). The figure is taken from [49].

4.3 Sub-surface imaging and the potential for nano-tomography

Probing of the depth profile of the permittivity of multilayer samples is discussed in Refs [63–65]. The goal is to unravel or to test the composition of samples with s-SNOM. The publications report measurements and numerical studies for the permittivity of multilayer specimens detected by s-SNOM. The calculations were performed based on full-wave simulations and general solutions of the wave equation by Green's functions. Based on the results, sub-surface tomography aiming at the determination of layer permittivities and thicknesses appears possible within limits if some prior knowledge exists about the composition of the samples. The probing depth is tens of nanometers.

The capability of THz s-SNOM to detect buried structures was reported in Ref. [69]. This represents a simpler task than multilayer tomography. Ref. [67] describes the application of a THz TDS s-SNOM to sense a Au grating embedded in a thin layer of Si_3N_4. The thickness of the nitride layer above the gold stripes varied, but amounted on average to 30 nm. The nitride layer had a smooth surface with the consequence that the topography did not reveal the Au grating, only the permittivity variations did.

Figure 5 depicts the scheme of the sample under the s-SNOM tip that is illuminated by THz pulses. **Figure 6** presents experimental data. Panels (a–c) show the 1st, 2nd and 3rd harmonic of the demodulated near-field signal, respectively. The maps reveal the pattern of the buried Au stripes with a spatial resolution of 90 nm. The contrast arises from the conductivity differences between Au and the insulators Si and Si_3N_4. **Figure 6d** presents the AFM image of the sample, simultaneously recorded with the s-SNOM images. The AFM map delivers no indication for the Au grating. Unlike Ref. [65], no attempt to quantify the depth of the grating based on the s-SNOM data was made. Similar studies were reported in [70], where a buried photonic resonator was studied in the near-IR/VISis spectral regime.

4.4 Direct mapping of surface waves

One of the applications of the s-SNOM technique is the direct observation of surface waves. Recently, Ref. [71] explored the existence of plasma waves in the channels of field-effect transistors (FETs). The excitation of such waves was predicted for the situation that a THz signal is applied either at the gate-drain or the gate-source port of the FET [72, 73]. FETs monolithically integrated with antennas are in use nowadays as detectors of THz radiation. The devices are mainly fabricated in Si CMOS or AlGaN/GaN foundry technology [74, 75]. However, as the

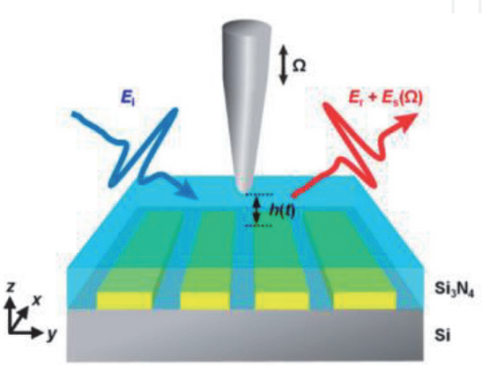

Figure 5.
Schematic of the sample-under-test consisting of periodically arranged Au stripes (thickness: 30 nm, period: 800 nm) embedded in Si_3N_4. The substrate is insulating Si. Reprinted with permission from [15]. Copyright (2021) American Chemical Society.

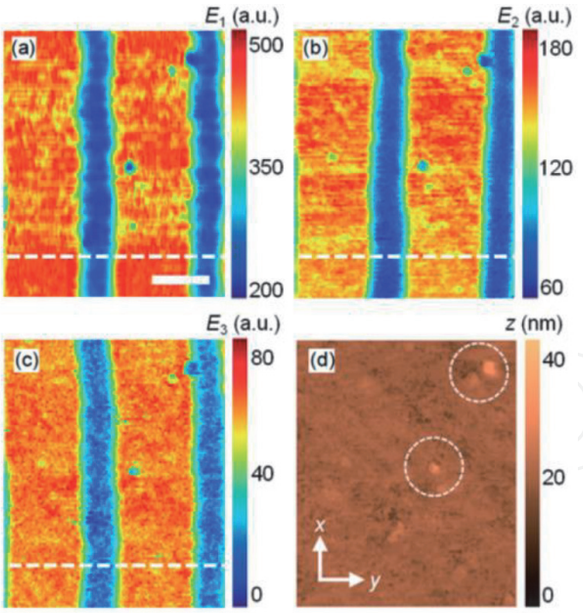

Figure 6.
1st-, 2nd-, and 3rd-harmonic s-SNOM signals (a–c) and an AFM topographical map (d) of the sample depicted in ***Figure 5****. Reprinted with permission from [15]. Copyright (2021) American Chemical Society.*

channels are buried under the gate metal, they are not suited for the direct probing of the predicted plasma waves by s-SNOM. Graphene, in contrast, allows for the fabrication of inverted FET structures, where the graphene channel lies on top of the gate.

Figure 7a shows an optical micrograph of a device under investigation in [69]. The graphene FET is located in the center of a THz bow-tie antenna, which is asymmetric for preferred injection of plasma waves from the source side upon THz illumination. **Figure 7b** presents an SEM image of the white box shown in **Figure 7a**. One can discern the graphene stripe on the gate electrode connecting the source and drain electrodes. **Figure 7c** shows a schematic of the device and the s-

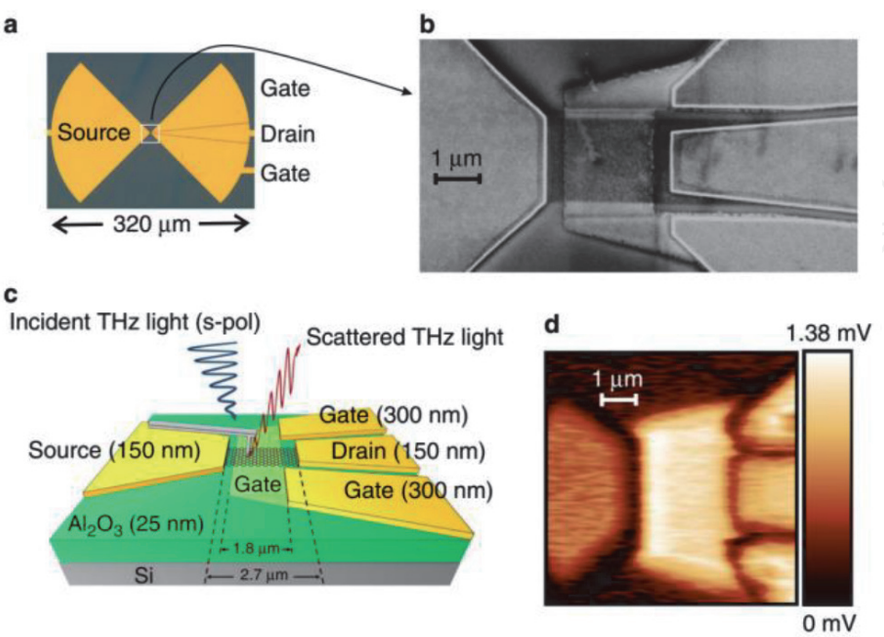

Figure 7.
(a) Optical micrograph of a graphene FET in a bow-tie antenna; (b) SEM image of the FET in the center of the device; (c) schematic of the device and the s-SNOM measurement; (d) near-field map of the electric field distribution derived by signal demodulation at the 2nd harmonic of the tip oscillation frequency. The figure is taken from [71].

SNOM measurement procedure. The device was illuminated by pulsed radiation at 2.0 THz from a FEL, the scattered radiation from the s-SNOM tip was detected with a liquid-helium-cooled InSb hot-electron bolometer. The s-SNOM was operated in self-homodyne mode. **Figure 7d** exhibits a recorded time-averaged electric-field map of the illuminated FET. The bright signal on the gate region has contributions of both the THz signal on the buried gate electrode, which is not fully screened by the graphene sheet, and of the overdamped plasma wave injected into the graphene from the left (source side, see brightest region over the first few hundred nanometers of the graphene stripe). The overdamped plasma wave decays in the graphene sheet over a distance of 0.3–0.5 μm. This is a considerably long propagation distance for the 25–70-fs lifetime of the plasma wave in the unprotected, not encapsulated, graphene sheet.

Another example of THz s-SNOM measurements of surface waves was recently reported in Ref. [76]. Here, the topic was the observation of phonon polaritons in the van der Waals semiconductor α-MoO_3, and the proof of their hyperbolic (self-confined) propagation in spectral regions where the dielectric permittivity is positive in one spatial direction and negative in another. The measurements were performed with pulsed FEL radiation between 8 to 12 THz and cryogenically cooled IR photodetectors. The s-SNOM was operated in self-homodyne mode with 2nd-harmonic demodulation.

5. Conclusion

In this chapter, we have reviewed the state of the art of near-field imaging with the s-SNOM technique at THz frequencies. s-SNOM is an established technique of nano-scale spectroscopy at visible and IR radiation frequencies, and only recently has been extended to longer wavelengths into the THz regime. The same spatial resolution of down to 10 nm is achieved as in the visible and IR spectral regimes. After an introduction of s-SNOM in sections 1 and 2, we have given in Section 3 an overview of the specific technical developments of THz s-SNOM, presenting in **Table 1** a timeline of major advances. Section 4 then has discussed four representative studies which stand for current application areas of THz s-SNOM in the research on solid-state materials and structures. The topics are the mapping of the electric conductivity, the imaging of phase transitions, sub-surface imaging, and the probing of surface waves.

Ref. (year)	Source	Detector	Resolution	Remarks
[77] (2003)	THz pulses	Bolometer EO sampling	150 *nm*	• Stationary tip above the sample
[78] (2007)	THz pulses	Photoconductive antenna	n/a	• Vibrating tip above the sample • Recorded data presented for 1st harmonic
[48] (2008)	THz pulses	EO sampling	n/a	• Self-etched tip • Higher harmonic demodulation
[5] (2008)	THz gas laser	Bolometer	40 *nm*	• Interferometric detection • 2.54 THz
[17] (2014)	THz pulses	Photoconductive antenna	90 *nm*	• Subsurface imaging
[53] (2016)	FEL	Bolometer	50 *nm*	• Broad band • High power • 1.3–8.5 THz

Ref. (year)	Source	Detector	Resolution	Remarks
[61] (2017)	THz gas laser	Graphene-based THz photodetector	n/a	• Tuning tip length in resonance • 3.11 THz
[19] (2017)	THz-QCL	THz-QCL	78 *nm*	• Quantum Cascade Laser self-mixing • Probe tip on a tuning fork • 2.85 THz
[79] (2018)	THz gas laser	Bolometer	∼20 *nm*	• Synthetic Optical Holography • 1.89 THz
[35] (2018)	Multiplier chain	Schottky diode (in waveguide)	50 *nm*	• All-electronic THz setup • Transceiver design • 0.5 to 0.75 THz • Heterodyne detection
[33] (2019)	THz gas laser	Schottky diode (in waveguide)	<15 *nm*	• Study the effect of the tip length and shape • 2.52 THz
[54] (2019)	Multiplier chain	Schottky diode (in waveguide)	1*μm*	• W band (110 GHz) • Large tip instead of commercial AFM tips
[18] (2020)	THz pulses	Photoconductive antenna	<100 *nm*	• Indium tip for a $\frac{\lambda}{2}$ resonance • Probe tip on a tuning fork • Optimized photoconductive antenna for detection
[80] (2020)	Optical and THz pulses	EO sampling	20 *nm*	• THz emission nanoscopy • 11-*nm*laser field confinement
[57] (2020)	THz-QCL	Photocurrent in device-under-test	35 *nm*	• CW THz-QCL as radiation source
[27] (2021)	Multiplier chain	Field-effect transistor (lens-coupled)	40 *nm*	• All-electronic THz setup • FET with monolithically integrated antenna • Phase-resolved homodyne detection • 246.5 GHz

Table 1.
Timeline of advances.

Acknowledgements

M.M. Wiecha acknowledges financial support from the Dr. Hans Messer Stiftung for his doctoral studies. Some of the work was supported by the Hessian Excellence Program LOEWE.

Author details

Matthias M. Wiecha, Amin Soltani* and Hartmut G. Roskos*
Physikalisches Institut, Goethe-Universität Frankfurt, Germany

*Address all correspondence to: soltani@physik.uni-frankfurt.de
and roskos@physik.uni-frankfurt.de

References

[1] Keilmann, F. FIR microscopy. Infrared Phys. Technol. **36**, 217–224 (1995).

[2] Richards, D. & Zayatas, A. *Nano-Optics and Near-Field Optical Microscopy*. (2008).

[3] Pohl, D. W., Denk, W. & Lanz, M. Optical stethoscopy: Image recording with resolution λ/20. Appl. Phys. Lett. **44**, 651–653 (1984).

[4] Keilmann, F. & Hillenbrand, R. Near-field microscopy by elastic light scattering from a tip. Philos. Trans. R. Soc. A Math. Phys. Eng. Sci. **362**, 787–805 (2004).

[5] Huber, A., Keilmann, F., Wittborn, J., Aizpurua, J. & Hillenbrand, R. Terahertz Near-Field Nanoscopy of Mobile Carriers in Single Semiconductor Nanodevices. Nano Lett. **8**, 3766–3770 (2008).

[6] Knoll, B., Keilmann, F., Kramer, A. & Guckenberger, R. Contrast of microwave near-field microscopy. Appl. Phys. Lett. **70**, 2667–2669 (1997).

[7] Tuca, S.-S., Kasper, M., Kienberger, F. & Gramse, G. Interferometer Scanning Microwave Microscopy: Performance Evaluation. IEEE Trans. Nanotechnol. **16**, 991–998 (2017).

[8] Baskakova, A., Stella, G. & Hoffmann, K. An Interferometric Sensor for Scanning Microwave Microscopy Application. in *2018 Asia-Pacific Microwave Conference (APMC)* vols 2018-Novem 1232–1234 (IEEE, 2018).

[9] Seo, M. A. *et al.* Fourier-transform terahertz near-field imaging of one-dimensional slit arrays: mapping of electric-field-, magnetic-field-, and Poynting vectors. Opt. Express **15**, 11781 (2007).

[10] Adam, A. J. L. *et al.* Advanced terahertz electric near-field measurements at sub-wavelength diameter metallic apertures. Opt. Express **16**, 7407 (2008).

[11] Kang, T., Bahk, Y.-M. & Kim, D.-S. Terahertz quantum plasmonics at nanoscales and angstrom scales. Nanophotonics **9**, 435–451 (2020).

[12] Seo, M. A. *et al.* Near field imaging of terahertz focusing onto rectangular apertures. Opt. Express **16**, 20484 (2008).

[13] Park, H.-R. *et al.* Colossal Absorption of Molecules Inside Single Terahertz Nanoantennas. Nano Lett. **13**, 1782–1786 (2013).

[14] Sawallich, S. *et al.* Photoconductive Terahertz Near-Field Detectors for Operation With 1550-nm Pulsed Fiber Lasers. IEEE Trans. Terahertz Sci. Technol. **6**, 365–370 (2016).

[15] Cocker, T. L., Peller, D., Yu, P., Repp, J. & Huber, R. Tracking the ultrafast motion of a single molecule by femtosecond orbital imaging. Nature **539**, 263–267 (2016).

[16] Cocker, T. L. *et al.* An ultrafast terahertz scanning tunnelling microscope. Nat. Photonics **7**, 620–625 (2013).

[17] Moon, K. *et al.* Subsurface Nanoimaging by Broadband Terahertz Pulse Near-Field Microscopy. Nano Lett. **15**, 549–552 (2015).

[18] Siday, T., Hale, L. L., Hermans, R. I. & Mitrofanov, O. Resonance-Enhanced Terahertz Nanoscopy Probes. *ACS Photonics* **7**, 596–601 (2020).

[19] Degl'Innocenti, R. *et al.* Terahertz Nanoscopy of Plasmonic Resonances with a Quantum Cascade Laser. ACS Photonics **4**, 2150–2157 (2017).

[20] Cvitkovic, A., Ocelic, N. & Hillenbrand, R. Analytical model for quantitative prediction of material contrasts in scattering-type near-field optical microscopy. Opt. Express **15**, 8550 (2007).

[21] McLeod, A. S. *et al.* Model for quantitative tip-enhanced spectroscopy and the extraction of nanoscale-resolved optical constants. Phys. Rev. B - Condens. Matter Mater. Phys. **90**, 085136 (2014).

[22] Esslinger, M. & Vogelgesang, R. Reciprocity Theory of Apertureless Scanning Near-Field Optical Microscopy with Point-Dipole Probes. ACS Nano **6**, 8173–8182 (2012).

[23] Esteban, R., Vogelgesang, R. & Kern, K. Tip-substrate interaction in optical near-field microscopy. Phys. Rev. B - Condens. Matter Mater. Phys. **75**, 1–8 (2007).

[24] Muller, J., Parent, G. & Lacroix, D. Tip optimization for improvement of detection in scanning near-field optical microscopy. J. Opt. **14**, 075703 (2012).

[25] HillenbRand, R., Knoll, B. & Keilmann, F. Pure optical contrast in scattering-type scanning near-field microscopy. J. Microsc. **202**, 77–83 (2001).

[26] Taubner, T., Hillenbrand, R. & Keilmann, F. Performance of visible and mid-infrared scattering-type near-field optical microscopes. J. Microsc. **210**, 311–314 (2003).

[27] Wiecha, M. M. *et al.* Antenna-coupled field-effect transistors as detectors for terahertz near-field microscopy. Nanoscale Adv. **3**, 1717–1724 (2021).

[28] Courjon, D., Bainier, C., Girard, C. & Vigoureux, J. M. Near field optics and light confinement. Ann. Phys. **505**, 149–158 (1993).

[29] García, R. Dynamic atomic force microscopy methods. Surf. Sci. Rep. **47**, 197–301 (2002).

[30] Knoll, B. & Keilmann, F. Enhanced dielectric contrast in scattering-type scanning near-field optical microscopy. Opt. Commun. **182**, 321–328 (2000).

[31] Raschke, M. B. & Lienau, C. Apertureless near-field optical microscopy: Tip–sample coupling in elastic light scattering. Appl. Phys. Lett. **83**, 5089–5091 (2003).

[32] Schmidt, P. *et al.* Nano-imaging of intersubband transitions in van der Waals quantum wells. Nat. Nanotechnol. **13**, 1035–1041 (2018).

[33] Maissen, C., Chen, S., Nikulina, E., Govyadinov, A. & Hillenbrand, R. Probes for Ultrasensitive THz Nanoscopy. ACS Photonics **6**, 1279–1288 (2019).

[34] Gomez, L. *et al.* Apertureless scanning near-field optical microscopy: a comparison between homodyne and heterodyne approaches. J. Opt. Soc. Am. B **23**, 823 (2006).

[35] Liewald, C. *et al.* All-electronic terahertz nanoscopy. Optica **5**, 159 (2018).

[36] Ocelic, N., Huber, A. & Hillenbrand, R. Pseudoheterodyne detection for background-free near-field spectroscopy. Appl. Phys. Lett. **89**, 101124 (2006).

[37] Moreno, C., Alda, J., Kinzel, E. & Boreman, G. Phase imaging and detection in pseudo-heterodyne scattering scanning near-field optical microscopy measurements. Appl. Opt. **56**, 1037 (2017).

[38] Huth, F. *et al.* Nano-FTIR Absorption Spectroscopy of Molecular Fingerprints at 20 nm Spatial Resolution. Nano Lett. **12**, 3973–3978 (2012).

[39] Qazilbash, M. M. *et al.* Infrared spectroscopy and nano-imaging of the insulator-to-metal transition in vanadium dioxide. APS **79**, (2009).

[40] Walla, F. *et al.* Anisotropic excitation of surface plasmon polaritons on a metal film by a scattering-type scanning near-field microscope with a non-rotationally-symmetric probe tip. Nanophotonics **7**, 269–276 (2018).

[41] Dai, S. *et al.* Tunable Phonon Polaritons in Atomically Thin van der Waals Crystals of Boron Nitride. *Science (80-.).* **343**, 1125–1129 (2014).

[42] Hu, F. *et al.* Imaging exciton–polariton transport in MoSe2 waveguides. Nat. Photonics **11**, 356–360 (2017).

[43] Basov, D. N., Fogler, M. M. & Garcia de Abajo, F. J. Polaritons in van der Waals materials. *Science (80-.).* **354**, aag1992–aag1992 (2016).

[44] Fei, Z. *et al.* Gate-tuning of graphene plasmons revealed by infrared nano-imaging. Nature **486**, 82–85 (2012).

[45] Chen, J. *et al.* Optical nano-imaging of gate-tunable graphene plasmons. Nature **487**, 77–81 (2012).

[46] Walla, F. *et al.* Near-Field Observation of Guided-Mode Resonances on a Metasurface via Dielectric Nanosphere Excitation. ACS Photonics **5**, 4238–4243 (2018).

[47] Zouaghi, W. *et al.* Broadband terahertz spectroscopy: principles, fundamental research and potential for industrial applications. Eur. J. Phys. **34**, S179–S199 (2013).

[48] von Ribbeck, H.-G. *et al.* Spectroscopic THz near-field microscope. Opt. Express **16**, 3430 (2008).

[49] Stinson, H. T. *et al.* Imaging the nanoscale phase separation in vanadium dioxide thin films at terahertz frequencies. Nat. Commun. **9**, 3604 (2018).

[50] Yang, Z. *et al.* Near-Field Nanoscopic Terahertz Imaging of Single Proteins. Small **17**, 2005814 (2021).

[51] Aghamiri, N. A. *et al.* Hyperspectral time-domain terahertz nano-imaging. Opt. Express **27**, 24231 (2019).

[52] Yoxall, E. *et al.* Direct observation of ultraslow hyperbolic polariton propagation with negative phase velocity. Nat. Photonics **9**, 674–678 (2015).

[53] Kuschewski, F. *et al.* Narrow-band near-field nanoscopy in the spectral range from 1.3 to 8.5 THz. Appl. Phys. Lett. **108**, 113102 (2016).

[54] Dai, G. *et al.* W-Band Near-Field Microscope. *IEEE Access* **7**, 48060–48067 (2019).

[55] Chen, X. *et al.* THz Near-Field Imaging of Extreme Subwavelength Metal Structures. ACS Photonics **7**, 687–694 (2020).

[56] Giordano, M. C. *et al.* Phase-resolved terahertz self-detection near-field microscopy. Opt. Express **26**, 18423 (2018).

[57] Pogna, E. A. A. *et al.* Unveiling the detection dynamics of semiconductor nanowire photodetectors by terahertz near-field nanoscopy. Light Sci. Appl. **9**, 189 (2020).

[58] Wang, H., Wang, L. & Xu, X. G. Scattering-type scanning near-field optical microscopy with low-repetition-rate pulsed light source through phase-domain sampling. Nat. Commun. **7**, 13212 (2016).

[59] Chen, C. *et al.* Terahertz Nanoimaging and Nanospectroscopy of

Chalcogenide Phase-Change Materials. ACS Photonics **7**, 3499–3506 (2020).

[60] Schnell, M., Carney, P. S. & Hillenbrand, R. Synthetic optical holography for rapid nanoimaging. Nat. Commun. **5**, 3499 (2014).

[61] Mastel, S. *et al.* Terahertz Nanofocusing with Cantilevered Terahertz-Resonant Antenna Tips. Nano Lett. **17**, 6526–6533 (2017).

[62] https://rmnano.com/.

[63] Govyadinov, A. A. *et al.* Recovery of Permittivity and Depth from Near-Field Data as a Step toward Infrared Nanotomography. ACS Nano **8**, 6911–6921 (2014).

[64] Mooshammer, F. *et al.* Quantifying Nanoscale Electromagnetic Fields in Near-Field Microscopy by Fourier Demodulation Analysis. ACS Photonics **7**, 344–351 (2020).

[65] Mester, L., Govyadinov, A. A., Chen, S., Goikoetxea, M. & Hillenbrand, R. Subsurface chemical nanoidentification by nano-FTIR spectroscopy. Nat. Commun. **11**, 3359 (2020).

[66] O'Callahan, B. T. *et al.* In Liquid Infrared Scattering Scanning Near-Field Optical Microscopy for Chemical and Biological Nanoimaging. Nano Lett. **20**, 4497–4504 (2020).

[67] Durmaz, Y. C., Goetz, A. & Keilmann, F. Infrared Nanoscopy of Alive Biological Cell Surfaces. in *2019 44th International Conference on Infrared, Millimeter, and Terahertz Waves (IRMMW-THz)* vols 2019-Septe 1–1 (IEEE, 2019).

[68] https://en.wikipedia.org/wiki/AFM-IR.

[69] Moon, K. *et al.* Subsurface nanoimaging by broadband terahertz pulse near-field microscopy. Nano Lett. **89**, 549–552 (2015).

[70] Mey, O. *et al.* Enhancement of the Monolayer Tungsten Disulfide Exciton Photoluminescence with a Two-Dimensional Material/Air/Gallium Phosphide In-Plane Microcavity. ACS Nano **13**, 5259–5267 (2019).

[71] Soltani, A. *et al.* Direct nanoscopic observation of plasma waves in the channel of a graphene field-effect transistor. Light Sci. Appl. **9**, 97 (2020).

[72] Dyakonov, M. & Shur, M. Detection, mixing, and frequency multiplication of terahertz radiation by two-dimensional electronic fluid. IEEE Trans. Electron Devices **43**, 380–387 (1996).

[73] Dyakonov, M. & Shur, M. Shallow water analogy for a ballistic field effect transistor: New mechanism of plasma wave generation by dc current. Phys. Rev. Lett. **71**, 2465–2468 (1993).

[74] Ikamas, K. *et al.* Broadband Terahertz Power Detectors Based on 90-nm Silicon CMOS Transistors With Flat Responsivity Up to 2.2 THz. *IEEE Electron Device Lett.* **39**, 1413–1416 (2018).

[75] Bauer, M. *et al.* A High-Sensitivity AlGaN/GaN HEMT Terahertz Detector With Integrated Broadband Bow-Tie Antenna. IEEE Trans. Terahertz Sci. Technol. **9**, 430–444 (2019).

[76] Oliveira, T. V. A. G. *et al.* Nanoscale-Confined Terahertz Polaritons in a van der Waals Crystal. Adv. Mater. **33**, 2005777 (2021).

[77] Chen, H. T., Kersting, R. & Cho, G. C. Terahertz imaging with nanometer resolution. Appl. Phys. Lett. **83**, 3009–3011 (2003).

[78] Zhan, H. *et al.* The metal-insulator transition in VO2 studied using

terahertz apertureless near-field microscopy. Appl. Phys. Lett. **91**, 162110 (2007).

[79] Mastel, S. *et al.* Understanding the Image Contrast of Material Boundaries in IR Nanoscopy Reaching 5 nm Spatial Resolution. ACS Photonics **5**, 3372–3378 (2018).

[80] Pizzuto, A., Mittleman, D. M. & Klarskov, P. Laser THz emission nanoscopy and THz nanoscopy. Opt. Express **28**, 18778 (2020).